Improving the performance of lead-free piezoelectric composites by using polycrystalline inclusions and tuning the dielectric matrix environment

Jagdish A Krishnaswamy[1] , **Federico C Buroni**[2], **Felipe Garcia-Sanchez**[3], **Roderick Melnik**[1,4], **Luis Rodriguez-Tembleque**[4] **and Andres Saez**[4]

[1] MS2Discovery Interdisciplinary Research Institute, Wilfrid Laurier University, 75 University Ave W, Waterloo, Ontario, N2L 3C5, Canada
[2] Department of Mechanical Engineering and Manufacturing, Universidad de Sevilla, Camino de los Descubrimientos s/n, Seville E-41092, Spain
[3] Department of Civil Engineering, Materials and Manufacturing, University of Malaga, Av. De Cervantes, 2, E-29016 Málaga, Spain
[4] Department of Continuum Mechanics and Structural Analysis, Universidad de Sevilla, Camino de los Descubrimientos s/n, Seville E-41092, Spain

E-mail: ajagdish@wlu.ca

CrossMark

Abstract

Piezoelectric composites are a class of smart materials which can be manufactured in a scalable manner by additive processes, while catering to a wide range of applications. Recent efforts are directed towards composites of lead-free piezoelectric materials with a goal of achieving performances comparable to lead-based composites. While there has been extensive research in fabrication methodologies such as 3D printing, which can manufacture complex piezoelectric structures in a scalable manner, there are important remaining questions as to how the performance of lead-free piezoelectric composites can be further improved. Fundamental to this is the understanding of key factors underlying piezoelectric performance: the electro-elastic interactions between the piezoelectric material and the matrix, the effects of the polycrystalline microstructure of the piezoelectric inclusions, the effect of randomly shaped polycrystalline fillers, and the effect of the volume fraction of the piezoelectric material in the matrix. A strong motivation for using polycrystalline fillers is that they can exhibit enhanced piezoelectric and mechanical properties compared to single crystalline materials. Moreover, polycrystalline materials are amenable to scalable manufacturing. We computationally investigate these important aspects of piezoelectric composite design and performance by taking into account for the first time the polycrystalline nature of lead-free piezoelectric inclusions, in the context of a matrix-inclusion composite. We achieve this by dispersing randomly shaped polycrystalline inclusions at random positions in the matrix which allows us to better understand the behavior of practical composite architectures. In such cases, our analysis reveals that although polycrystalline piezoelectric materials, in isolation, can outperform their single crystal counterparts, in a composite architecture these enhancements are not straightforward. We identify the sources of loss which prevent polycrystalline inclusions from enhancing the performance of the composites. By tuning the dielectric environment in the matrix through the inclusion of metallic nanoparticles, we demonstrate how the performance of the composites can be further significantly improved. Specifically, when the metal nanoparticles are near the percolation threshold, we show that polycrystalline piezoelectric inclusions perform better than

single crystals, with an improvement of around 14.6% in the effective piezoelectric response. We conclude that such novel architectures, devised by a combination of polycrystalline piezoelectric inclusions in a high permittivity environment, can improve the performance of the composites beyond the single crystal design and thus offer a promising direction for 3D printable lead-free piezoelectric composites.

(Some figures may appear in colour only in the online journal)

1. Introduction

Sensing and harvesting energy available in the environment in the form of mechanical stimuli using piezoelectric materials and devices is an important aspect of many emerging engineering applications. These include integrated structural health monitoring [1], sensing, and wearable health care, to name just a few [2]. However, most of the currently deployed devices are based on lead-based materials which pose environmental concerns at the manufacturing stage, usage, as well as at the final stage of improper disposal [2]. Therefore, the focus of recent research has been to design and manufacture piezoelectric devices and composites based on lead-free materials. It is also important to note that even in the case of some classes of lead-free piezoelectric materials, such as KNN (Potassium Sodium Niobate), their mining and extraction may pose considerable detrimental impact on the environment [3]. Although the piezoelectric response of such materials can be significantly improved through atomic doping [4], the synthesis of the materials entails a heavy environmental cost. Hence, it is important to judiciously select piezoelectric materials which are both lead-free and environmentally friendly in their processing. In this paper, we focus on the composites of lead-free material Barium Titanate ($BaTiO_3$), although our developed computational framework is applicable to other materials too. The timely relevance of $BaTiO_3$ and related materials is apparent through recent development of accelerated material discovery using emerging machine learning algorithms [5], through recent efforts in development of $BaTiO_3$-based piezoelectric composites [6–9], as well as through novel applications of these materials [10]. Importantly, these composites can be fabricated in a scalable manner using emerging manufacturing methods such as 3D printing [11–13] and $BaTiO_3$ can be synthesized using facile eco-friendly methods [14].

Piezoelectric composites are an interesting class of smart materials which incorporate a dispersion of nanoscale and/or microscale piezoelectric materials inside a matrix. These materials and devices based on them are particularly effective in sensing or harvesting energy from irregular mechanical stimuli such as random vibration, bending, twisting, folding, and pressing, and so on. Such devices can be easily integrated with structures ranging from civil infrastructure such as buildings, aircraft parts, to the human body in the form of soft implants which harvest biomechanical stimuli [2]. The practical interest in these materials and devices stems from the ease of design and scalable fabrication using additive manufacturing techniques [12, 13, 15–17]. The inclusion of nanoscale materials also offers the possibility to harvest energy with superior efficiencies due to the processes that are important at the nanoscale such as the flexoelectric effect, where large strain gradients arising due to small dimensions also lead to generation of electric flux [18–21].

Currently the computer-aided design of such composites uses single crystal electro-elastic coefficients [22–24]. These calculations typically use the homogenization approach which attempts to obtain effective macroscale properties taking into account the variations that occur at smaller length scales. The homogenization approach defines a macroscale representative volume element (RVE) which is a volume of a composite containing sufficient information to model the statistical spread in the electro-elastic properties at the microscale [25]. The RVE is then used to obtain the effective electro-elastic properties of the heterogeneous composite. The importance of this approach is that the homogenized properties of the composite computed this way can further be used in the design of larger structures, by using the homogenized RVE as a repeated building block, and prediction of their electro-elastic behavior, thus allowing multiscale design [23]. However, currently the associated calculations overlook important effects which arise due to the microscale polycrystalline structure of the piezoelectric material that is embedded in the matrix. In fact, experimental observations point out that the grain size effects in piezoelectric polycrystals play an important role in determining the efficiency of piezoelectric response [26], and that there exist ideal grain sizes, typically in the submicron scale, which maximize the piezoelectric response in bulk polycrystals. Besides, polycrystals offer additional degrees of freedom in the design, where we can tune the mechanical properties of the material. They are easier to synthesize, offering excellent quality control [27]. Therefore, it is important to include these additional effects, mentioned above, in the modeling of piezoelectric composites in order to generate refined models which take into account the polycrystalline structure of the piezoelectric material in a generic fashion. Theoretical studies on bulk materials have shown that there are significant variations in the electro-elastic coefficients that occur as a function of the orientation of grains within a polycrystal [27, 28]. These investigations also show that optimal polycrystallinity, in isolated piezoelectric polycrystals, can lead to piezoelectric performances that are superior to single crystal behavior [27, 28]. It is of interest to understand if polycrystallinity-induced enhancement can be harnessed in a piezoelectric composite. In this paper, we develop such refined models for piezoelectric matrix-inclusion composites taking into account the polycrystalline microstructure through an orientation distribution parameter, which will determine the effective

electro-elastic coefficients of polycrystalline piezoelectric ceramics [27]. By applying our developed computational framework, we will also analyze the effect of the shape of the microscale polycrystalline inclusions, exploring consequences of randomly shaped inclusions and the volume fraction of such inclusions. Our analysis will be centered on two kinds of matrices—a soft matrix which is characteristic of flexible wearable devices, and a harder matrix which is characteristic of structure-integrated devices. The matrices we consider here fit within the context of 3D printable materials, because they are solution-processed materials which harden on curing [29, 30]. First, this allows us to explore the design of piezoelectric composites across a range of deployment scenarios. Secondly, at a more fundamental level of material design, this allows us to understand the role of the mechanical characteristics of the matrix in determining the piezoelectric response of the composite. Furthermore, this can help identify if there is a need to tune the mechanical and electrical properties of the matrix to maximize the response, by using nanoscale or microscale additives with appropriate electro-elastic characteristics. Using our observations from these studies, we demonstrate a proof-of-concept composite design where a combination of optimally polycrystalline piezoelectric inclusions in a matrix, providing an optimally tuned dielectric environment results in improved performance and surpassing the performance of single crystal composite designs. Given the ease of processing of the materials considered here, these novel designs can be effectively realized by using scalable techniques such as solution processing, mechanical mixing, and 3D printing, making important contributions towards environmentally-friendly piezoelectric composite technology.

The paper is organized as follows. In section 2, we provide details of the coupled electro-elastic model, the composite geometry and associated boundary conditions, as well as of the material property models which are used in our computational framework. In section 3, we present the results of our analysis of polycrystal-based piezoelectric composites including a novel design which demonstrates enhanced piezoelectric activity in polycrystal-based structures compared to their counterparts with single-crystal based composites. Section 4 summarizes our findings and concludes the paper.

2. Coupled electro-elastic model

We consider a two-dimensional matrix-inclusion composite architecture at steady state. We model the composite using linear piezoelectric theory. In what follows, we briefly explain the mathematical aspects of the model.

2.1. Basic relationships

The electrical and mechanical fields are linearly coupled as follows [22, 31]

$$\sigma_{ij}(\mathbf{x}) = c_{ijkl}^E(\mathbf{x})\varepsilon_{kl}(\mathbf{x}) - e_{ijk}(\mathbf{x})E_k(\mathbf{x}), \quad (1)$$

$$D_j(\mathbf{x}) = e_{jkl}(\mathbf{x})\varepsilon_{kl}(\mathbf{x}) + \epsilon_{jk}^S(\mathbf{x})E_k(\mathbf{x}). \quad (2)$$

Here σ_{ij} and ε_{ij} are the elastic stresses and strains respectively, D_j are the components of the electric flux density vector, E_k are the components of the electric field vector, c_{ijkl}, e_{ijk}, and ϵ_{ij} are the elastic coefficients, piezoelectric coefficients, and the dielectric permittivity coefficients and $\mathbf{x}$ is (x_1, x_3). The superscripts E and S signify that the coefficients are measured at constant electric field and constant strain, respectively. The strain field is related to the gradient of the displacement vector field $\mathbf{u}(\mathbf{x})$ by the Cauchy relationship:

$$\varepsilon_{ij} = \frac{1}{2}(u_{i,j}(\mathbf{x}) + u_{j,i}(\mathbf{x})). \quad (3)$$

The electric field is related to the gradient of the electric potential as

$$E_i(\mathbf{x}) = -\phi_{,i}(\mathbf{x}). \quad (4)$$

For the two-dimensional model considered here, the equations (1), (2) are simplified into the following, by using the Voigt notation [22]:

$$\begin{bmatrix} \sigma_{11} \\ \sigma_{33} \\ \sigma_{13} \end{bmatrix} = \begin{bmatrix} c_{11} & c_{13} & 0 \\ c_{13} & c_{33} & 0 \\ 0 & 0 & c_{44} \end{bmatrix} \begin{bmatrix} \varepsilon_{11} \\ \varepsilon_{33} \\ \varepsilon_{13} \end{bmatrix} - \begin{bmatrix} 0 & e_{31} \\ 0 & e_{33} \\ e_{15} & 0 \end{bmatrix} \begin{bmatrix} E_1 \\ E_3 \end{bmatrix}, \quad (5)$$

$$\begin{bmatrix} D_1 \\ D_3 \end{bmatrix} = \begin{bmatrix} 0 & 0 & e_{15} \\ e_{31} & e_{33} & 0 \end{bmatrix} \begin{bmatrix} \varepsilon_{11} \\ \varepsilon_{33} \\ \varepsilon_{13} \end{bmatrix} + \begin{bmatrix} \epsilon_{11} & 0 \\ 0 & \epsilon_{33} \end{bmatrix} \begin{bmatrix} E_1 \\ E_3 \end{bmatrix}. \quad (6)$$

2.2. Equilibrium conditions and governing equations

Equations (1)–(4) are further subject to conditions of equilibrium and Gauss's law with the assumption of vanishing body forces and vanishing volume charge density. These are given by

$$\sigma_{ij,j}(\mathbf{x}) = 0, \quad (7)$$

$$D_{i,i}(\mathbf{x}) = 0. \quad (8)$$

The phenomenological relationships in equations (1), (2), subject to the assumption-based relationships in equations (3), (4) and the governing equations (7), (8), describe the steady state behavior of the electro-elastic system. The well-posedness of such models of coupled piezoelectricity, along with rigorous energy bounds, were derived by one of us in a series of earlier papers, e.g. [32]. This was done for the first time even in a more general, dynamic setting, through the application of the Faedo–Galerkin procedure and generalized solution technique. In our present analysis, this model has been implemented and simulated with the finite element method in the context of matrix-inclusion geometries specified next.

2.3. Composite geometry and boundary conditions

We consider a two-dimensional model in the x_1–x_3 plane. We model an RVE shown schematically in figure 1. We incorporate randomly shaped microscale piezoelectric inclusions at random positions within a matrix with sides a_m and b_m.
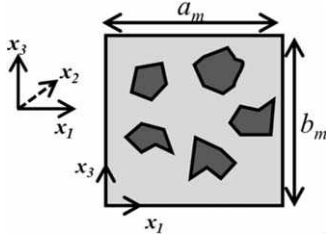
Figure 1. Schematic of the piezoelectric composite RVE with randomly shaped polycrystalline piezoelectric inclusions randomly dispersed in a square matrix. The axis system used in the study is also illustrated.

Table 1. Geometrical parameters exemplified in the simulations.

Geometrical parameter	Value (μm)
Matrix	
a_m	50
b_m	50
Inclusions (bound within two concentric circles of radii R_1 and R_2, chosen randomly)	
R_1 range	2.5–3.5
R_2 range	4.0–5.0

Table 1 summarizes the geometrical parameters of the matrix and the inclusions used in the simulations. Specifically, our results are exemplified for randomly shaped microscale inclusions at random positions inside of a square-shaped matrix with sides 50 μm long. These length scales are chosen in accordance with experimental observations of 3D-printed piezoelectric composites [13] and optimal grain sizes for enhanced piezoelectricity in polycrystals [26]. Our focus is on the study of composites with micro-structured piezoelectric inclusions dispersed in a microscale matrix. The algorithm used for generating the randomly shaped inclusions is given in appendix B.

In evaluating the piezoelectric response of such composites, we calculate the effective e_{31} and e_{33} of the composite for which we apply two sets of boundary conditions [22]. These are shown in figures 2(a) and (b), respectively, and summarized in appendix C. Using boundary conditions BC1, we calculate the effective properties, e_{11}^{eff}, c_{11}^{eff}, and c_{13}^{eff}, of the composite. Using the second set of boundary conditions BC2, we calculate the effective properties e_{33}^{eff}, c_{33}^{eff}, and c_{13}^{eff} of the composite. In the following calculation, the volume average of a quantity A is represented as $\langle A \rangle$ and is calculated as

$$\langle A \rangle = \frac{1}{a_m b_m} \int_\Omega A d\Omega, \tag{9}$$

where Ω is the volume over which the integration is carried out, which in this case is the total volume of the RVE.

Under boundary conditions BC1, we obtain the following volume averages

$$\langle \varepsilon_{11} \rangle = \overline{\varepsilon_{11}}, \ \langle \varepsilon_{33} \rangle = 0, \ \langle \varepsilon_{13} \rangle = 0, \ \langle E_i \rangle = 0. \tag{10}$$

The following effective coefficients of the composite are subsequently obtained as [22]

$$e_{31}^{eff} = \frac{\langle D_3 \rangle}{\overline{\varepsilon_{11}}}, \ c_{11}^{eff} = \frac{\langle \sigma_{11} \rangle}{\overline{\varepsilon_{11}}}, \ c_{13}^{eff} = \frac{\langle \sigma_{33} \rangle}{\overline{\varepsilon_{11}}}, \tag{11}$$

where $\langle D_3 \rangle$ is the volume average of the D_3 component of the electric flux density vector. Similarly, by using the second set of boundary conditions BC2, we obtain the following volume averages

$$\langle \varepsilon_{11} \rangle = 0, \ \langle \varepsilon_{33} \rangle = \overline{\varepsilon_{33}}, \ \langle \varepsilon_{13} \rangle = 0, \ \langle E_i \rangle = 0. \tag{12}$$

Subsequently, the following effective coefficients of the composite are calculated as

$$e_{33}^{eff} = \frac{\langle D_3 \rangle}{\overline{\varepsilon_{33}}}, \ c_{33}^{eff} = \frac{\langle \sigma_{33} \rangle}{\overline{\varepsilon_{33}}}, \ c_{13}^{eff} = \frac{\langle \sigma_{11} \rangle}{\overline{\varepsilon_{33}}}. \tag{13}$$

In our calculations, we assume small strains and accordingly set $\overline{\varepsilon_{11}}$ and $\overline{\varepsilon_{33}}$ in BC1 and BC2, respectively, to 1×10^{-6}.

2.4. Material models

Details of the material properties of the composites are given next. Firstly, we provide details on the mechanical and dielectric properties of the non-piezoelectric matrix materials. Next, we discuss our models for the effective electro-elastic coefficients of polycrystalline BaTiO$_3$ as a function of the grain orientation distribution.

2.4.1. Matrix models. We consider soft and hard non-piezoelectric matrices to cover two different scenarios of deployment. Both these matrices are isotropic in their mechanical and dielectric behavior. Soft matrices such as PDMS, PEGDA and so on are required in the context of wearable devices [13, 33]. Harder matrices are typically employed in piezoelectric sensors which are integrated with structures [22, 34]. These matrix materials are characterized by two parameters—the Young's modulus E_m and the Poisson's ratio ν_m. Using these quantities, the elastic coefficients of the matrix materials are given by

$$\mathbf{C_m} = \begin{bmatrix} \lambda_m + 2\mu_m & \lambda_m & \lambda_m & 0 & 0 & 0 \\ \lambda_m & \lambda_m + 2\mu_m & \lambda_m & 0 & 0 & 0 \\ \lambda_m & \lambda_m & \lambda_m + 2\mu_m & 0 & 0 & 0 \\ 0 & 0 & 0 & \mu_m & 0 & 0 \\ 0 & 0 & 0 & 0 & \mu_m & 0 \\ 0 & 0 & 0 & 0 & 0 & \mu_m \end{bmatrix}, \tag{14}$$

where

$$\lambda_m = \frac{E_m \nu_m}{(1 + \nu_m)(1 - 2\nu_m)}, \ \mu_m = \frac{E_m}{2(1 + \nu_m)}. \tag{15}$$

Table 2 summarizes the material constants of two matrices for which computations have been carried out—the soft matrix PDMS (hereafter referred to as Matrix M$_1$), and the relatively harder matrix—araldite LY5052 (hereafter referred to as Matrix M$_2$). Matrix material M$_2$ is a chemically
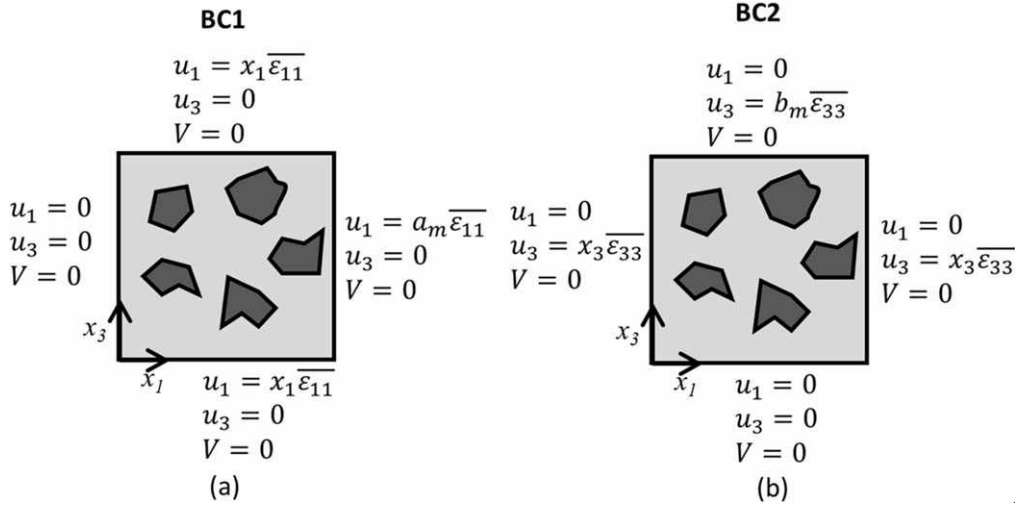
Figure 2. Two sets of boundary conditions (a) BC1 and (b) BC2, used to calculate the effective electro-elastic coefficients of the composite.

Table 2. Mechanical and dielectric properties of the matrix materials used in this study.

Material constant	M1: PDMS (soft matrix) [29]	M2: Araldite LY5052 (hard matrix) ([35] and datasheets)
Tensile modulus, E_m (Pa)	2×10^6	3.5×10^9 (from datasheet)
Poisson's ratio, ν_m	0.499	0.35 (from datasheet)
Relative permittivity		
ϵ_{11}/ϵ_0	2.72	3.5 [35]
ϵ_{33}/ϵ_0	2.72	3.5

Table 3. Mechanical, piezoelectric, and dielectric properties of single crystal $BaTiO_3$ used in this study.

Material constants	Values
Elastic coefficients (Pa)	
c_{11}^E	275.1×10^9
c_{13}^E	151.55×10^9
c_{33}^E	164.8×10^9
c_{44}^E	54.3×10^9
Relative permittivity	
$\epsilon_{11}^S/\epsilon_0$	1970
$\epsilon_{33}^S/\epsilon_0$	109
Piezoelectric coefficients (C m^{-2})	
e_{15}	21.3
e_{31}	−2.69
e_{33}	3.65

robust solution cast epoxy which is routinely used in structural parts. These matrices are representative of many similar materials which have similar properties. The additional rationale in considering these materials lies in the fact that they are both cast in the liquid state which allows for their easy processing by such techniques as solution processing, mixing, 3D printing and so on.

2.4.2. Inclusion models. The piezoelectric inclusions have electro-elastic coefficients which are functions of the polycrystalline microstructure. In what follows, we highlight the key features of the model that derives the polycrystalline electro-elastic coefficients starting from single-crystal data, assuming that each grain has the properties of the single crystal with respect to its local basis. In the derivation of the effective homogenized properties of the polycrystals, we assume that the composite is poled along the x_3 direction, across the cross section of the composite architecture, as typically observed in experiments [11]. The model will thus take into account the random orientation distribution within the polycrystals, after poling, with respect to the reference x_3 axis, along which ideally all the *c*-axes of the $BaTiO_3$ unit cells are expected to align. Such polycrystalline models are important in the light of experimental

observations which show considerable deviations in the electro-elastic coefficients as a function of the poling conditions [36]. Table 3 summarizes the material constants of the single crystal $BaTiO_3$ piezoelectric inclusion used here [27, 37]. These measurements show good agreement with other reported measurements in the literature [38]. The polycrystal material properties are derived from these values. As seen from table 3, the elastic coefficients are measured at constant electric field (marked by superscript *E*) and the permittivity coefficients at constant strain (marked by superscript *S*). Therefore, the derived coefficients of polycrystalline $BaTiO_3$ inclusions also correspond to similar conditions of measurement.

We assume a transversely isotropic distribution of grains with the isotropy axis coincident with the x_3 axis. This distribution is given by a Gaussian dependence on the Euler angle θ of the *c* axis of a grain about the x_3-axis. It is

important to note that the orientation distribution is also a function of a parameter α, which quantifies the degree of orientation in a poled piezoelectric polycrystal [27]. As α tends to zero, the Gaussian distribution narrows down and the electro-elastic coefficients tend to the single crystal values. At the other extreme, when α tends to infinity, the grains are randomly oriented. In particular, the piezoelectric activity of a polycrystal ceases, because of randomly oriented domains canceling out the electric fluxes within the polycrystal. The orientation distribution function (ODF) is given by [27]

$$W(\theta, \varphi, \phi) = \frac{1}{\alpha\sqrt{2\pi}} e^{-\frac{\theta^2}{2\alpha^2}}. \quad (16)$$

The ODF is generally a function of the three Euler angles θ, φ, and ϕ. However, owing to the traverse isotropy of the polycrystals, the dependence is only on θ. Using this ODF, the effective properties of the polycrystal are obtained from

$$\langle H \rangle = \int_0^{2\pi} \int_0^{2\pi} \int_{-1}^{1} H(\xi, \varphi, \phi) W(\xi, \varphi, \phi) d\xi d\varphi d\phi, \quad (17)$$

where $\xi = \cos(\theta)$ and H represents a generic crystal tensorial property. It is noteworthy, that it is a challenge to experimentally determine the ODF, evidenced by the availability of only a few recent efforts attempting to reconstruct the ODF [39] using specialized experiments. However, the texture coefficients, that consequently result due to the ODF, can usually be determined experimentally, subject to the limitations of the experimental technique [27]. It is also important to note that the ODF takes into account the orientation of the grains with respect to a reference direction (resulting from the poling field applied after the fabrication of the composite) and is thus polar in nature. We refer to [27] for the details of the development of a model to determine electro-elastic coefficients of the polycrystalline inclusion as a function of the distribution of grain orientations. The inclusions are assumed to be transversely isotropic along the x_1–x_3 plane. The texture coefficients obtained from literature (in our case [27]) are interpolated (see appendix D for the plots) and the resulting electro-elastic coefficients are shown in figures 3(a)–(c), as a function of the orientation parameter α. The orientation parameter α gives the effective properties of the polycrystal, thus taking into account microscale variations in the grain orientation, and consequently refining the electro-elastic model with a more accurate prediction of microscale properties of the composite. This self-consistent model assumes that each grain behaves as a single crystal with respect to its local coordinate system, implicating that all the domains inside a grain have similar orientations. Thus, the parameter α in the ODF holds the information on the polarity of the polycrystalline inclusions after the composite is poled. In the context of the composite architecture, the value of α importantly depends on two factors—the processing conditions under which the piezoelectric polycrystals are synthesized prior to their inclusion in the matrix, and the electric field applied during the poling after the preparation of the composite. Good processing conditions can yield highly textured polycrystals or also
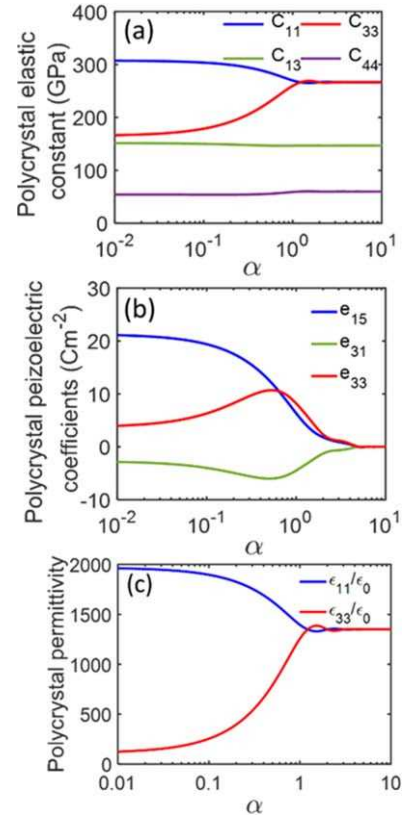

Figure 3. The electro-elastic coefficients of polycrystalline BaTiO$_3$ as a function of the orientation parameter α obtained using a Gaussian grain orientation distribution function of equation (16).

single crystals which are highly oriented in a preferred direction [40]. The electric field applied during the poling of the composite can further cause net alignment of domains within a grain in a preferred direction [27]. Together these factors result in a net value of α which describes the deviation from the ideally oriented and poled ceramic inclusions. Detailed data which establish the dependence of α on experimental conditions are, unfortunately, absent. However, the predicted isotropic elastic moduli of randomly oriented BaTiO$_3$ (i.e. for $\alpha \rightarrow \infty$ in figure 3(a)) agree reasonable well with the measured isotropic elastic moduli ($c_{11}^E = 204$ GPa and $c_{13}^E = 110$ GPa) of unpoled BaTiO$_3$ [36]. Additionally, α can also depend on the quality of the interface formed between the matrix and the inclusion, which is evident from the observed improvement in the piezoelectric response on establishing a covalent linkage at the matrix-inclusion interface [13]. In this paper, we assume that the composite is poled along the x_3 direction. Seen in this light, the limiting case of $\alpha \rightarrow \infty$ corresponds to an unpoled inclusion with a high degree of randomness in its grain orientations. The inclusion is, therefore, isotropic in its properties for this limiting case and thus exhibits no piezoelectric activity.

3. Results and discussion

We consider six composites with increasing volume fraction V_p occupied by the piezoelectric inclusions. These are
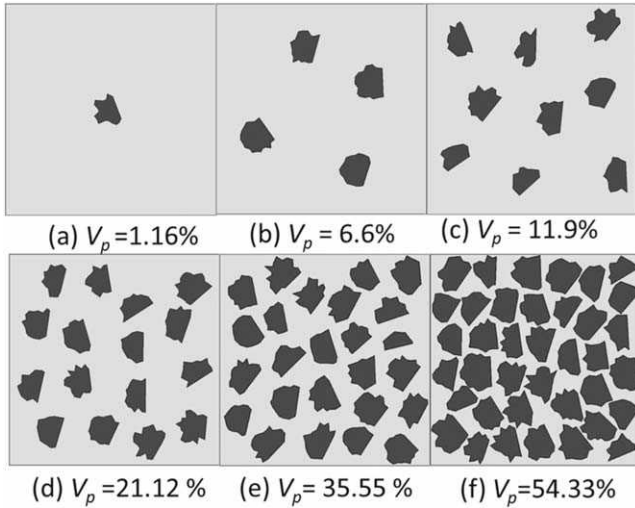
Figure 4. The six RVEs used in our computations in the increasing order of the inclusion volume fraction V_p from (a) to (f). The number of random polycrystalline inclusions, N, in (a)–(f) are 1, 4, 9, 16, 25, and 38, respectively.

illustrated in figures 4(a)–(f) with the corresponding volume fractions. Statistical tests to ensure convergence were carried out for a range of volume fractions V_p and the number of inclusions N, by considering five different RVEs for each (N, V_p). In all the cases, the means, standard deviations, and covariances were calculated. The covariances were of the order of 10^{-2} for both the effective elastic and the piezoelectric coefficients, thus implying a small statistical spread, which is also not very sensitive to the random shapes and positions of the inclusions.

A limiting case of 400 inclusions in an RVE of sides 200 μm was considered for the volume fraction, V_p, of 35.55% (corresponding to the smaller RVE with the same volume fraction, seen in figure 4(e)) to mimic a large RVE ($N \rightarrow \infty$). On comparing the results of the RVE in figure 4(e) with this limiting case, the relative errors in calculating the piezoelectric coefficients and the elastic coefficients were of the order of 10^{-2} and 10^{-3}, respectively. This analysis clearly shows that the RVEs considered for our study exhibit convergent results over the range of N and V_p considered here. It is to be noted that the RVEs considered here assume that the piezoelectric inclusions are not in contact. While physical contacts between the inclusions can indeed improve the piezoelectric response via better coupling of applied strain through the inclusions, the goal of the design strategies developed in the present work is to improve the piezoelectric response under conditions where the inclusion concentration is not high enough to cause a physical contact.

We first look at the piezoelectric coefficients of the composites with polycrystalline piezoelectric inclusions. We plot the effective piezoelectric coefficients as a function of the polycrystal orientation distribution parameter, α, and the volume fraction, V_p, occupied by the inclusions in the RVE. Figures 5(a) and (d) show the effective coefficient e_{31} of the matrices M_1 and M_2. We observe that the absolute values of the effective e_{31} are higher in matrix M_2 which has a higher

modulus of elasticity compared to M_1. It is thus concluded that a harder matrix, which allows for a better channeling of strain into the piezoelectric inclusion, results in better piezo-electric performance. The magnitude of the effective coefficient e_{31}, in both matrices, increases with increasing the inclusion volume fraction V_p and decreasing polycrystallinity α. Therefore, in designing composite architectures with either of these matrices, it would be beneficial to have inclusions which are highly crystalline. This is made even more clear from the analysis of the plots presented for fixed inclusion volume fraction $V_p = 35.6\%$ in figures 5(b) and (e) in the cases of matrices M_1 and M_2, respectively. It is noteworthy that the two matrices exhibit opposite trends, with matrix M_1 having a positive and M_2 having negative effective coefficient e_{31}. This occurs due to the opposite nature of the average strain $\langle \varepsilon_{33} \rangle$ that develops within the inclusions in the two matrices. In matrix M_1, the average ε_{33} in the inclusions is positive and in matrix M_2 it is negative for all α. This is seen even better in the figure 5(g) which shows $\langle \varepsilon_{33} \rangle$ in the composites with 38 inclusions when the boundary conditions BC1 are applied. This is expected due to the largely different Poisson's ratios of the two matrices. Indeed, matrix M_1, which has a large Poisson's ratio, causes larger tensile stress σ_{33} in the inclusions, thus reversing the direction of the effective polarization compared to the matrix M_2. It is seen that by tuning the elastic properties of the matrix, the direction of the effective piezoelectric parameters can be switched. For a given α, it is also observed from the analysis of figures 5(c) and (f) that higher inclusion volume fractions lead to better performing effective coefficients e_{31}.

Next, we look at the effective coefficient e_{33} of the composites. Figures 6(a) and (d) show the behavior of e_{33}^{eff} for the two matrices as a function of α and V_p. From the effective properties of a single polycrystalline piezoelectric structure, as shown by the data in figure 3(c), it is intuitive to expect that polycrystalline inclusions with α just below 1, should exhibit enhanced e_{33}^{eff} compared to single crystal inclusions. However, the composite behavior does not fit this intuitive pattern and e_{33}^{eff} drops with increasing α (figures 6(b) and (e)), indicating again that single crystalline inclusions could be better performing in such composite architecture designs. This is because as α increases, the effective coefficient c_{33} of the polycrystalline inclusion also increases (figure 3(a)). This reduces the average strain $\langle \varepsilon_{33} \rangle$ in the inclusions as seen from figure 6(g). Since the strain drops off with increasing polycrystallinity, the effective piezoelectric coefficient e_{33} also drops. However, this situation could be improved by designing matrices with enhanced electro-mechanical properties, which, in turn, could lead to the design of composites where the polycrystallinity may further contribute to improved piezoelectric responses. As seen from figures 6(c) and (f), the effective coefficient e_{33} of the composite improves as the volume fraction V_p of the inclusions increases, for a given value of α.

The effective elastic coefficients of the composites with matrices M_1 and M_2 are shown in figures 7(a)–(c) and (d)–(f), respectively. It is seen that the elastic properties of the composites are not as significantly affected by the polycrystallinity parameter α as for a stand-alone polycrystalline inclusion of
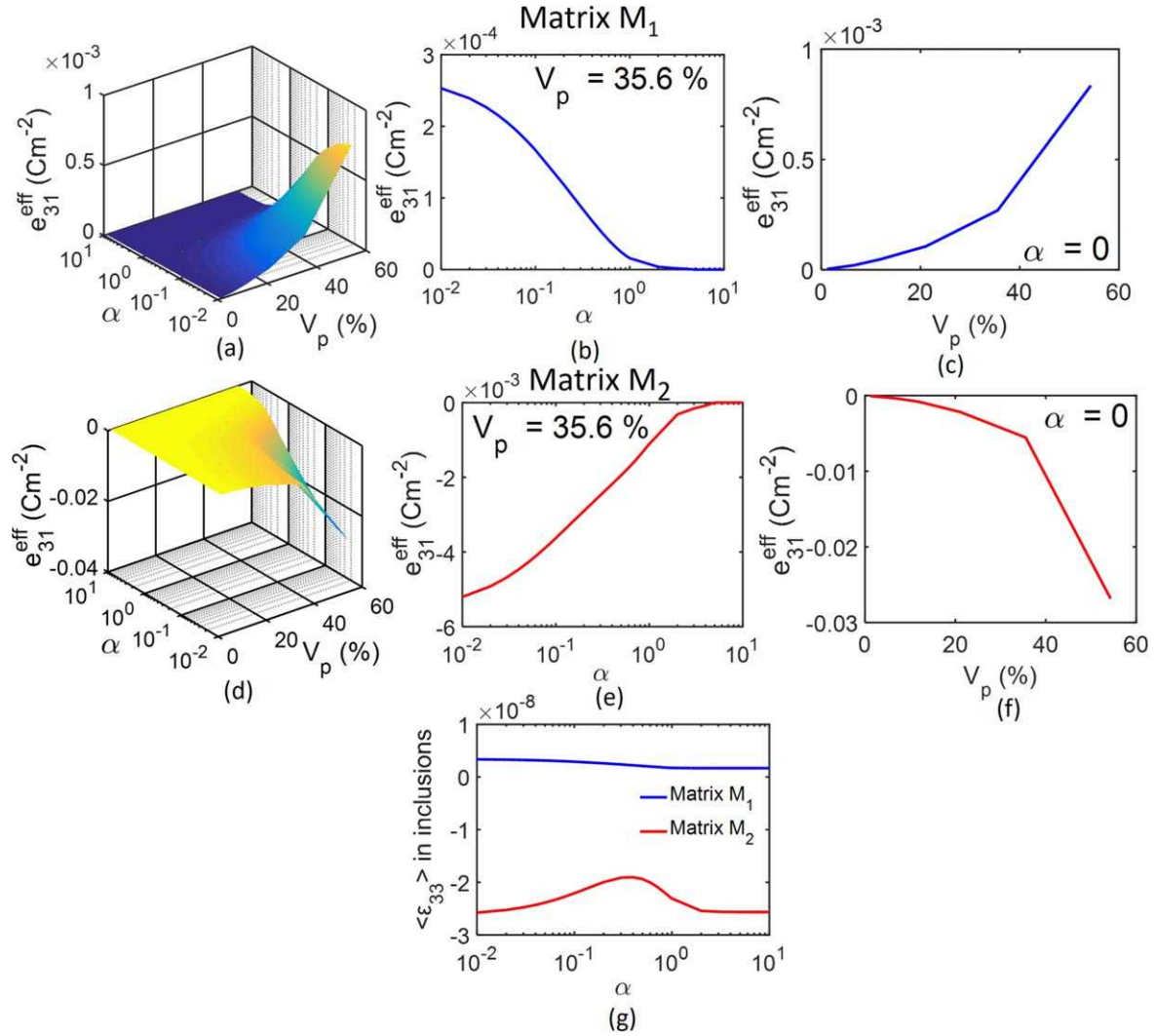
Figure 5. The effective coefficient e_{31} as a function of inclusion volume fraction V_p and the polycrystallinity factor α, plotted for composites with (a)–(c) Matrix M1, (d)–(f) Matrix M2. Subplots (b), (c) and (e), (f), respectively, show the effective coefficient e_{31} for $V_p = 35.6\%$ (and various α) and $\alpha = 0$ (and various V_p). Subplot (g) presents the volume averaged strain ε_{33} in the inclusions for the composite architecture with 38 inclusions (see figure 4(f)).

BaTiO$_3$. The variation in the elastic properties is sensitive to only the volume fraction V_p of the inclusions. This is because the matrix materials, which have elastic coefficients on the orders of magnitude smaller than those of the inclusions, outweigh the variations in the coefficients occurring due to polycrystalline effects. As seen in these figures, the effective parameters of the matrix M$_2$ with higher Young's modulus are higher than those of matrix M$_1$. The effective elastic coefficients increase, as intuitively expected, as the volume fractions V_p of the inclusions increases.

These findings indicate that although a polycrystalline piezoelectric material exhibits better piezoelectric performance, specifically as seen through improved e_{33} in pristine polycrystals without matrices, the composite architecture does not allow a similar straightforward improvement. This represents a challenge in the design of such composite architectures using lead-free piezoelectric polycrystals. Given that polycrystalline piezoelectric composites are well-suited materials for large scale piezoelectric devices, we address this

challenge next. One of the important ways to do that would be to synthesize and incorporate highly oriented piezoelectric polycrystals as seen in [40] and mimic single crystal piezoelectric domain behavior, while retaining the improved mechanical strength of the polycrystal. Clearly, in parallel to that, exploring new ways to improve the performance of composites with polycrystalline inclusions beyond that of composites based on single crystals represents both practical and fundamental interests. Further, such design approaches are important to obtain higher piezoelectric responses while still retaining low to moderate inclusion concentrations, which would be crucial for applications requiring soft composites. For example, as seen from literature [4], it is possible to obtain higher piezoelectric responses with high inclusion concentrations ($V_p > 80\%$). The calculations carried out here are for much lower inclusion concentrations, and thus we see at least an order of magnitude smaller effective coefficients compared to the composites with higher inclusion concentrations [4].
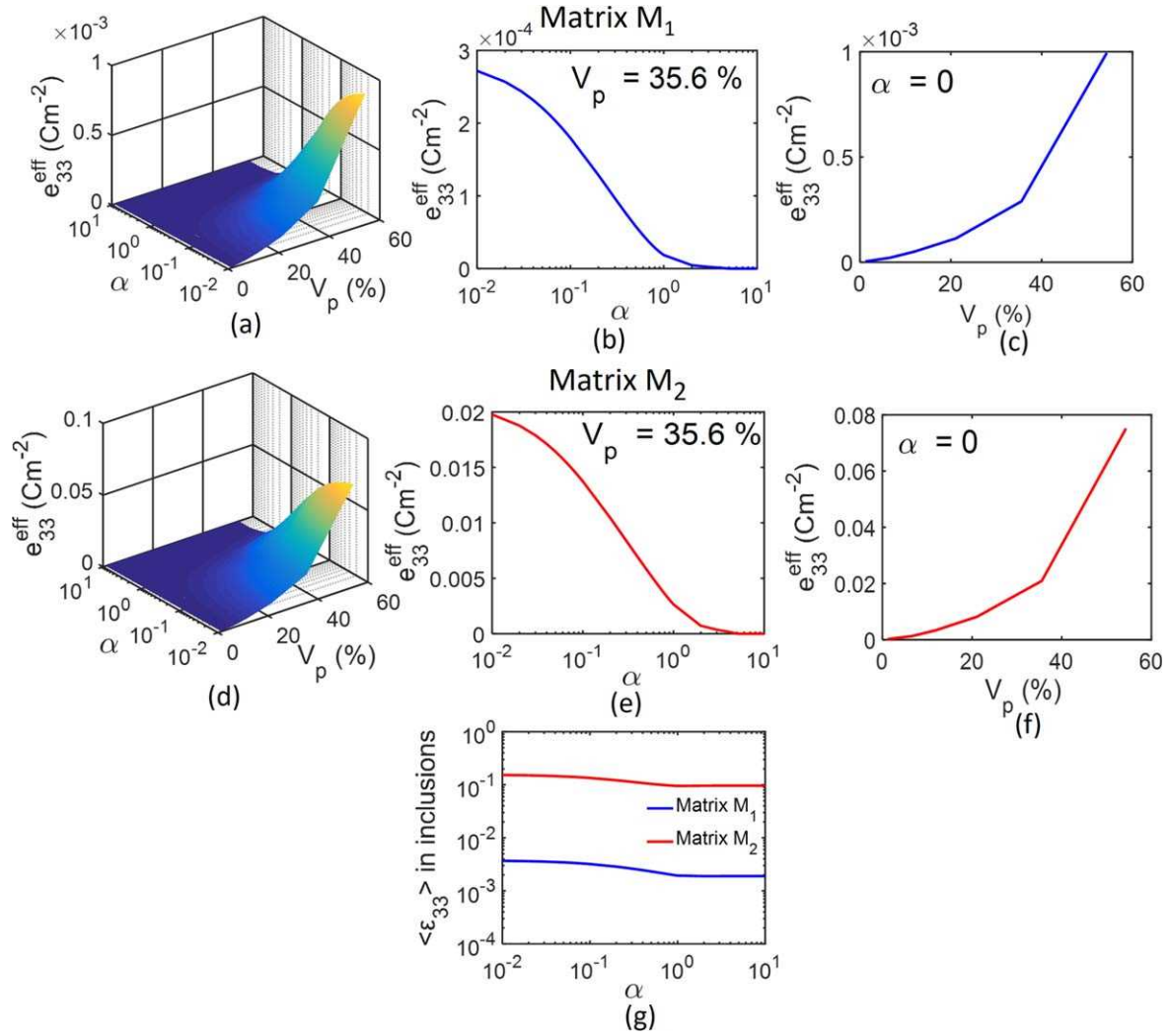
Figure 6. The effective coefficient e_{33} as a function of inclusion volume fraction V_p and the polycrystallinity factor α, plotted for composites with (a)–(c) Matrix M_1, (d)–(f) Matrix M_2. Subplots (b), (c) and (e), (f), respectively, show the effective e_{33} for $V_p = 35.6\%$ (and various α) and $\alpha = 0$ (and various V_p). Subplot (g) presents the volume averaged strain ε_{33} in the inclusions in the architecture with 38 inclusions (see figure 4(f)).

Therefore, in the remainder of the paper, we now use our findings to demonstrate a proof-of-concept design in which polycrystalline inclusions can outperform single-crystal-based designs in a composite architecture. Further, the design strategies developed here will aim to obtain piezoelectric responses comparable to composites with higher inclusion concentrations, while still retaining lower V_p. Polycrystals, which are better than single crystals in isolation (especially in their e_{33} response near $\alpha = 1$), do not perform better than single crystals in a composite. There are two main obstacles here. The first is 'mechanical' in nature as it arises due to the relative hardening of the inclusion with higher polycrystallinity. This prevents it from taking larger strains, by offloading the strain to the matrix, and thus reduces the effective piezoelectric property.

We have demonstrated this in the previous section (see figure 6(g)). The second obstacle lies with the fact that the weak dielectric environment provided by the matrix poses an electrical 'bottleneck' that does not allow the electric flux, generated within the inclusions, to propagate freely outward

through the composite. Therefore, the question we embark on is whether it is possible to widen the electrical 'bottleneck' by tuning the dielectric properties of the matrix without affecting the mechanical properties of the matrix. We consider the softer matrix M_1 which has weak piezoelectric behavior. By including silver nanoparticles in the matrix, the permittivity of the matrix can be increased by over two orders of magnitude [41]. When metallic nanoparticles are uniformly dispersed in a matrix of permittivity ϵ_m, the effective permittivity of the modified matrix increases.

Quantitatively, the effective permittivity, ϵ_m^{eff}, of the modified matrix with metal nanoparticles dispersed below their percolation threshold (figure 8), is given by a homogenized model [42], as

$$\epsilon_m^{eff}(f) = \epsilon_m \left(\frac{f_c}{f_c - f_{NP}} \right)^p, \qquad (18)$$

where f_{NP} is the fill fraction (synonymously, volume fraction) of the filler metal nanoparticles in the matrix, f_c is the critical
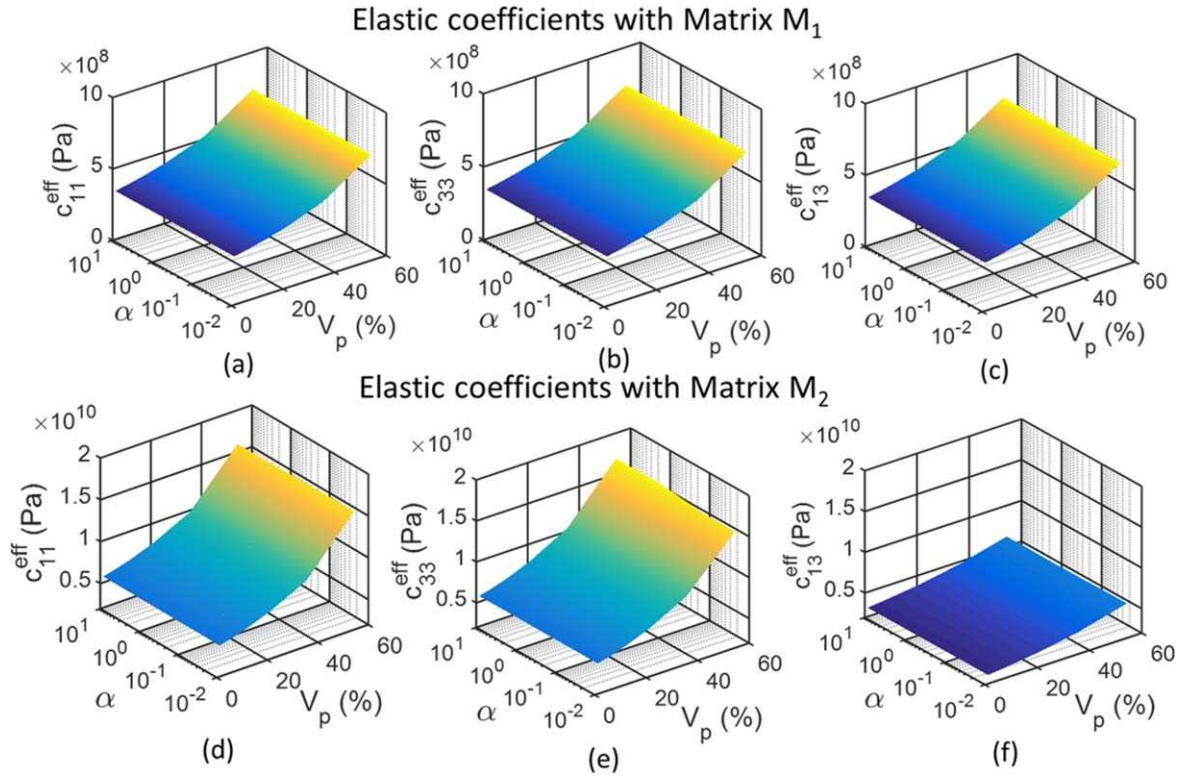
Figure 7. The effective elastic coefficients of composites with matrix M_1: (a)–(c) and matrix M_2: (d)–(f).
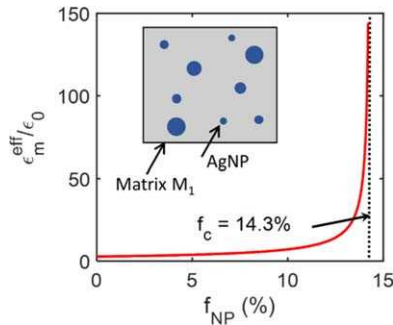

Figure 8. The relative permittivity of matrix M_1 as a function of the volume fraction of Ag nanoparticles (AgNP) in the matrix (the vertical line marks the percolation threshold). The inset schematically shows Ag nanoparticles of random sizes distributed within the matrix M_1.

fill fraction, known as the percolation threshold, and p is a material dependent fitting parameter. If f_{NP} exceeds f_c the originally non-conducting matrix becomes metallic due to the percolated network of contacts that gets established between the metal nanoparticles. We restrict our analysis to values of f_{NP} below and near f_c. Following [41], we obtain $f_c = 14.3\%$ and $p = 0.8$ for the matrix M_1 loaded with silver nanoparticles of sub-100 nm size with an average particle size of around 35 nm. Since, the size scales of these particles are much smaller compared to the size of the piezoelectric inclusions (roughly 10 μm as seen in table 1), the dielectric properties of the matrix are assumed to have a homogeneous effect on the inclusions. The effective relative permittivity of the matrix as a function of the fill fraction f_{NP} of silver

nanoparticles is shown in figure 8, with the inset schematically illustrating the random distribution of silver nanoparticles, of random size, within the matrix. It is emphasized here that adding conductive nanofillers to insulating matrices should be carried out carefully to avoid dielectric breakdown in the matrix. Depending on the matrix used, the dielectric breakdown strength of the matrix might limit the maximum f_{NP}, to maintain the interparticle distances larger than the critical spacings that might lead to breakdown [43].

We now calculate the effective coefficients e_{31} and e_{33} of the composite with polycrystalline piezoelectric inclusions, taking the composite architecture of figure 4(f), with $V_p = 54.33\%$, as a representative example. The effective coefficients e_{31} and e_{33} of the composites are plotted in figures 9(a) and (d), respectively, as a function of the nanoparticle fill fraction f_{NP} and the polycrystallinity factor, α. Firstly, these plots clearly show that irrespective of α, the modification of the matrix with metal nanoparticles results in dramatic improvements in the effective piezoelectric response. This is made clear by a slice of the effective coefficients e_{31} and e_{33}, shown in figures 9(b) and (e), respectively, for $f_{NP} = 10\%$. We can clearly see that improvements in excess of 100%, in both the effective coefficients e_{31} and e_{33}, are possible in this particular exemplary case of $f_{NP} = 10\%$. These improvements are higher for higher nanoparticle fill fractions, as seen from figures 9(a) and (d). Furthermore, when f_{NP} approaches f_c, i.e. when the matrix is loaded with metallic nano-particles near percolation, we made the following observation. Figures 9(c) and (f) show two slices of effective coefficients e_{31} (figure 9(c)) and e_{33} (figure 9(f)), relative with respect to their respective values at
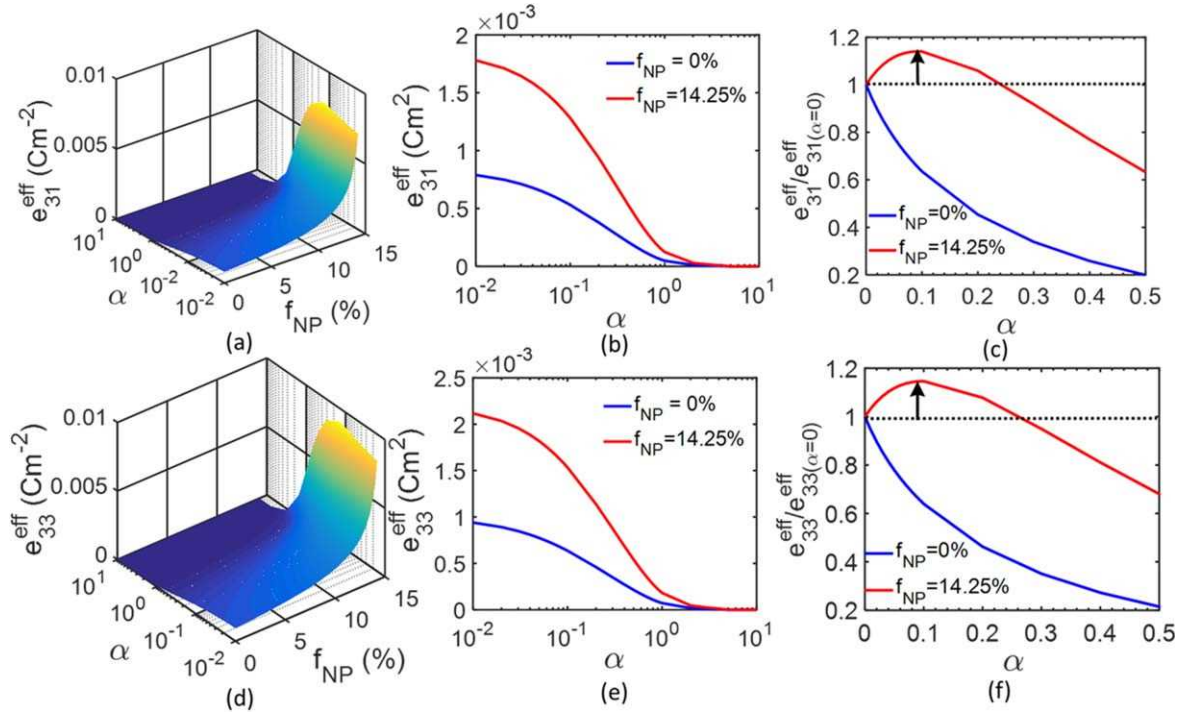
Figure 9. Piezoelectric enhancement in polycrystal-based composites using a metal nanoparticle-modified matrix with higher permittivity. These calculations are for $V_p = 54.33\%$ (corresponding to the RVE in figure 4(f)): subplots (a) and (d) show the effective coefficients e_{31} and e_{33}, respectively, of the composite as a function of the polycrystal parameter α and the AgNP fill fraction f_{NP}. Subplots (b) and (e) show the effective coefficients e_{31} and e_{33}, respectively, of the composite for $f_{NP} = 0\%$ and 10%. Subplots (c) and (f) show the effective coefficients e_{31} and e_{33}, respectively, of the composites with pristine and modified matrices (by AgNP), relative to their respective values at $\alpha = 0$.

$\alpha = 0$, for $f_{NP} = 0\%$ (pristine matrix) and $f_{NP} = 14.25\%$ (near percolation), as a function of α. The analysis of these results allows us to conclude that near the percolation threshold of metallic nanoparticles, the electrical 'bottleneck' mentioned above has been widened. Polycrystals with α roughly around 0.1 show enhancements in both the effective coefficients e_{31} and e_{33} compared to the composites with single crystals, with approximately 14% and 14.6% improvements, respectively, in this proof-of-concept demonstration. Furthermore, we note that bare polycrystals show a maximum in e_{33} for α of around 1, and in the composite this value of α has shifted to 0.1. Evidently, this maximum shifts to other values of α in other composite depending on the electrical and mechanical environment. From the perspective of composite design, this reveals that we can tune the matrix environment in terms of its mechanical moduli and permittivity to suit a particular polycrystalline inclusion. This is a considerable design advantage that relaxes the requirements on the piezoelectric crystal quality, processing conditions of the polycrystals, and the poling conditions of the composite, and thus warrants further investigations, both theoretical and experimental. Further, the improved piezoelectric responses (figures 9(a) and (d)) are almost comparable to the response of elastomer-matrix-based composites with very high inclusion loading ($V_p > 80\%$) [4], thus demonstrating that considerable performance improvements are possible with lower inclusion concentrations. This allows the design of composites with tailored mechanical properties and enhanced piezoelectric

responses to suit the requirements of niche applications such as wearable electronics, flexible integrated piezoelectric devices and so on. This is because of the significantly reduced hardening of the composite, which might be a problem at higher V_p, specifically in the context of applications such as in flexible or wearable electronics. This proof-of-concept demonstration of enhanced piezoelectric composite design shows that even in very soft matrices, which hinder the piezoelectric effect by shielding the inclusions from applied strain, tuning the dielectric permittivity of the matrix can help enhance the piezoelectric response. These findings further emphasize that there could be conditions under which a controlled randomness in the orientation of grains can lead to a better piezoelectric response compared to a fully oriented configuration. An extension of this design through the introduction of other nanomaterial inclusions, such as carbon nanotubes, which can simultaneously stiffen the matrix and improve its effective permittivity, can lead to even larger enhancements.

In summary, we have identified some of the key design rules that dictate the performance of lead-free matrix-inclusion piezoelectric composites. In particular, we demonstrated that in order to harness the superior behavior of polycrystalline piezoelectric inclusions, it is necessary to simultaneously tune the dielectric environment provided by the matrix. Conversely, the dielectric environment of the matrix could be possibly tuned to suit the requirements of a particular polycrystalline microstructure. This opens novel avenues for the

design of superior piezoelectric composites which are based on polycrystalline inclusions that can be synthesized relatively easily. Additionally, the methods of performance enhancement considered here are readily scalable, providing important inputs to the design of practical high-performance composites which can be manufactured by emerging technologies such as 3D printing. Finally, we expect that the key findings reported here are also relevant to the design of high-performance composites with piezoelectric matrices, such as PVDF, as well as with auxetic matrices.

4. Conclusions

We have developed a computational framework for the design of lead-free piezoelectric matrix-inclusion composites by accounting for the first time the polycrystalline nature of the BaTiO$_3$ piezoelectric inclusions with random shapes. We have demonstrated that while a polycrystal by itself could have better piezoelectric coefficients compared to a single crystal, this property is not directly transferrable to a composite architecture. Using our findings, we have highlighted a proof-of-concept design, wherein by optimally tuning the dielectric environment in the matrix with inclusion of metallic nanoparticles, composites based on polycrystalline inclusions outperform composites based on single crystal inclusions. These findings provide important insights into the role of randomness in the grain-orientation for the performance of piezoelectric composites, and in particular, how a controlled randomness in the orientation of polycrystalline inclusions can, under certain conditions, exhibit better performances compared to composites with highly oriented or single crystal inclusions. Consequently, these new design insights provide important inputs to additive manufacturing methods which can fabricate piezoelectric composites with optimal performance in a scalable manner.

Acknowledgments

Appendices

A.1. Generation of random shapes for polycrystalline inclusions

The random shapes were generated using a MATLAB code. The algorithm for the generation of the random shapes is given below

Step 1—Select a random number of sides n for the polygon to be generated in the range [n_1, n_2].

Step 2—Select random angle θ_0 between 0° and 90°. Select the range of random radii R_1 and R_2 defining the concentric circles within which the random shape will be spatially bounded. The center of these circles is the origin of the local coordinate system.

Step 3—Select an initial R_0 in the range [$R_{\min}$, $R_{\max}$]. The first vertex of the random object is defined in the local coordinates as (R_1, θ_1), where the reference origin is at the center of the random concentric circles.

Step 4—The next vertex of the polygon is at (R_2, θ_2) (in general (R_i, θ_i)) in the local coordinate system, which is obtained by a random incremental rotation by an angle θ, about the local origin, which is in the range [10°, $\theta_{\max} = 360/n$], and a random selection of the radius R in the range [R_1, R_2]. Joining the points (R_{i-1}, θ_{i-1}) and (R_i, θ_i) by a straight line, to form the ith edge of the polygon.

Step 5—Repeat step 4 till the total rotation adds up to 360°. Now there are '$n+1$' sets of coordinates. It is to be ensured that (R_0, θ_0) = (R_n, θ_n). Join these points by a straight line to get the nth edge of the polygon.

Parameters used in the study:

For each inclusion, the number of sides, n, of the polygonal inclusion, is chosen in step one, randomly in the range [n_1, n_2], where

n_1: 10.

n_2: 20.

Also the two bounding concentric circles within which the inclusion is spatially bounded, have radii R_1 and R_2 which are randomly selected as follows:

R_1: randomly chosen between 2.5 and 3.5 μm.

R_2: randomly chosen between 4 and 5 μm.

This gives polycrystals of rough sizes not exceeding 10 μm. i.e. the inclusions are spatially bounded within concentric circles of average radii 3 and 4.5 μm. This microscale dimension allows the accommodation of multiple grains, of sub-micron dimensions, within the inclusion. Therefore, the selection of the inclusion dimensions takes into account polycrystalline structures with submicron grain sizes which are experimentally observed to result in best piezoelectric responses [26].

A.2. Boundary conditions, effective coefficients, and computational details

There are two boundary conditions used in the calculations—BC1 and BC2 as highlighted schematically in figure 2. The following table summarizes the boundary condition and the corresponding effective parameters of the composite which are calculated through its application.

Boundary condition	Effective parameter calculated
BC1	c_{11}^{eff}, c_{13}^{eff}, e_{31}^{eff}
BC2	c_{33}^{eff}, c_{13}^{eff}, e_{33}^{eff}

The computations were carried out with a maximum element size of 1 μm. Regions at the random boundaries between the inclusion and the matrix were well resolved with smaller elements to reproduce the sharp transitions and

where $Z_{lmn}(\xi)$ is the generalized Legendre function [27] and $i = \sqrt{-1}$. We have obtained the analytical expressions for the normalized texture coefficients when the ODF is given by the Gaussian distribution function (16):

$$W_{100} = \frac{\sqrt{\frac{3}{2}}\, e^{-\frac{3\alpha^2}{2}}\left(\text{erf}\left(\frac{\pi - 2i\alpha^2}{\sqrt{2}\,\alpha}\right) - \text{erf}\left(\frac{\pi + 2i\alpha^2}{\sqrt{2}\,\alpha}\right) + 2i\,\text{erfi}(\sqrt{2}\,\alpha)\right)}{8\pi^2\left(\text{erf}\left(\frac{\pi - i\alpha^2}{\sqrt{2}\,\alpha}\right) - \text{erf}\left(\frac{\pi + i\alpha^2}{\sqrt{2}\,\alpha}\right) + 2i\,\text{erfi}\left(\frac{\alpha}{\sqrt{2}}\right)\right)}, \tag{AE1}$$

$$
\begin{aligned}
W_{200} = {}& -\frac{\sqrt{\frac{5}{2}}\, e^{-4\alpha^2}}{32\pi^2\left(\text{erfi}\left(\frac{\alpha^2 - i\pi}{\sqrt{2}\,\alpha}\right) + \text{erfi}\left(\frac{\alpha^2 + i\pi}{\sqrt{2}\,\alpha}\right) - 2\,\text{erfi}\left(\frac{\alpha}{\sqrt{2}}\right)\right)} \\
& \times \left(-3i\,\text{erf}\left(\frac{\pi - 3i\alpha^2}{\sqrt{2}\,\alpha}\right) + 3i\,\text{erf}\left(\frac{\pi + 3i\alpha^2}{\sqrt{2}\,\alpha}\right) + ie^{4\alpha^2}\left(\text{erf}\left(\frac{\pi - i\alpha^2}{\sqrt{2}\,\alpha}\right)\right.\right. \\
& \left.\left. - \text{erf}\left(\frac{\pi + i\alpha^2}{\sqrt{2}\,\alpha}\right) + 2i\,\text{erfi}\left(\frac{\alpha}{\sqrt{2}}\right)\right) + 6\,\text{erfi}\left(\frac{3\alpha}{\sqrt{2}}\right)\right), \tag{AE2}
\end{aligned}
$$

curvature effects induced by the random geometry of the inclusion. The results were convergent even for much smaller meshes, compared to the microscale dimensions of the inclusions, with maximum element sizes of 250 nm. Mesh refinements were carried out to specifically improve the resolution of the meshing at the sharp vertices of the polygons. The final minimum and maximum element sizes of 10 nm and 1 μm respectively, allowed for a mesh which optimally resolved sharp interfacial features between the inclusion and the matrix.

A.3. The texture coefficients of polycrystalline BaTiO$_3$

We used interpolation with splines to obtain the texture coefficients of polycrystalline BaTiO$_3$, from [27]. The interpolated coefficients are shown in figure A1. The effective electro-elastic coefficients of polycrystalline BaTiO$_3$ are obtained from the expressions given in [27] which incorporate these texture coefficients. These coefficients are highly sensitive to the orientation parameter α. When α tends to zero, the polycrystal resembles a highly oriented single crystal, and when α tends to infinity, the polycrystal is randomly oriented.

For completeness, we have also also derived analytical expressions for the texture coefficients W_{lmn} using the following expression, given in [27]

$$W_{lmn} = \int_0^{2\pi}\int_0^{2\pi}\int_{-1}^{+1} W(\xi,\ \varphi,\ \phi)Z_{lmn}(\xi)e^{im\varphi}e^{in\phi}d\xi d\varphi d\phi,$$

$$
\begin{aligned}
W_{300} = {}& -\frac{\sqrt{\frac{7}{2}}\, e^{-\frac{15\alpha^2}{2}}}{64\pi^2\left(\text{erfi}\left(\frac{\alpha^2 - i\pi}{\sqrt{2}\,\alpha}\right) + \text{erfi}\left(\frac{\alpha^2 + i\pi}{\sqrt{2}\,\alpha}\right) - 2\,\text{erfi}\left(\frac{\alpha}{\sqrt{2}}\right)\right)} \\
& \times \left(2ie^{6\alpha^2}\left(\text{erf}\left(\frac{\pi - 2i\alpha^2}{\sqrt{2}\,\alpha}\right) - \text{erf}\left(\frac{\pi + 2i\alpha^2}{\sqrt{2}\,\alpha}\right) + 2i\,\text{erfi}(\sqrt{2}\,\alpha)\right)\right. \\
& \left. - 5i\left(\text{erf}\left(\frac{\pi - 4i\alpha^2}{\sqrt{2}\,\alpha}\right) - \text{erf}\left(\frac{\pi + 4i\alpha^2}{\sqrt{2}\,\alpha}\right) + 2i\,\text{erfi}(2\sqrt{2}\,\alpha)\right)\right), \tag{AE3}
\end{aligned}
$$

and

$$
\begin{aligned}
W_{400} = {}& \frac{3e^{-12\alpha^2}}{512\sqrt{2}\,\pi^2\left(\text{erf}\left(\frac{\pi - i\alpha^2}{\sqrt{2}\,\alpha}\right) - \text{erf}\left(\frac{\pi + i\alpha^2}{\sqrt{2}\,\alpha}\right) + 2i\,\text{erfi}\left(\frac{\alpha}{\sqrt{2}}\right)\right)} \\
& \times \left(2e^{12\alpha^2}\left(\text{erf}\left(\frac{\pi - i\alpha^2}{\sqrt{2}\,\alpha}\right) - \text{erf}\left(\frac{\pi + i\alpha^2}{\sqrt{2}\,\alpha}\right) + 2i\,\text{erfi}\left(\frac{\alpha}{\sqrt{2}}\right)\right)\right. \\
& + 15e^{8\alpha^2}\left(\text{erf}\left(\frac{\pi - 3i\alpha^2}{\sqrt{2}\,\alpha}\right) - \text{erf}\left(\frac{\pi + 3i\alpha^2}{\sqrt{2}\,\alpha}\right) + 2i\,\text{erfi}\left(\frac{3\alpha}{\sqrt{2}}\right)\right) \\
& \left. - 35\left(\text{erf}\left(\frac{\pi - 5i\alpha^2}{\sqrt{2}\,\alpha}\right) - \text{erf}\left(\frac{\pi + 5i\alpha^2}{\sqrt{2}\,\alpha}\right) + 2i\,\text{erfi}\left(\frac{5\alpha}{\sqrt{2}}\right)\right)\right) \tag{AE4}
\end{aligned}
$$

with erf($\cdot$) and erfi($\cdot$) denoting the Gauss error function and the imaginary Gauss error function respectively.
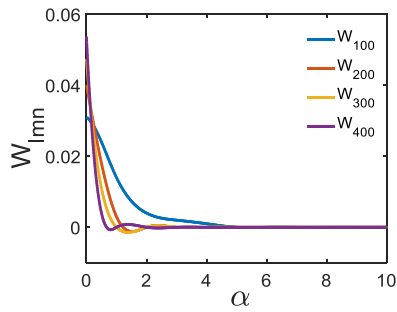
Figure A1. The orientation coefficients W_{lmn} obtained from [27] by interpolation with splines as a function of the polycrystalline orientation parameter α.
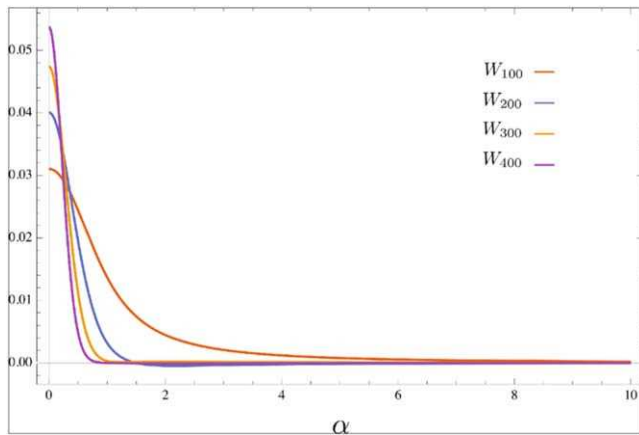

Figure A2. Plots of the texture coefficients obtained from analytical expressions (AE1)–(AE4).

These texture coefficients are highly sensitive to the orientation parameter α as shown in figure A1. When α tends to zero, the polycrystal resembles a highly oriented single crystal, and the texture coefficients become

$$W_{100} = \frac{\sqrt{\frac{3}{2}}}{4\pi^2}, \tag{AE5}$$

$$W_{200} = \frac{\sqrt{\frac{5}{2}}}{4\pi^2}, \tag{AE6}$$

$$W_{300} = \frac{\sqrt{\frac{7}{2}}}{4\pi^2}, \tag{AE7}$$

$$W_{400} = \frac{3}{4\sqrt{2}\,\pi^2}. \tag{AE8}$$

The plots of W_{lmn} obtained through the analytical expressions (AE1)–(AE4) are shown in figure A2. For the limiting case of $\alpha \to 0$, a Dirac delta function has been used as the ODF and single crystal electro-elastic parameters were successfully recovered. The analytical results in figure A2 are in good agreement with data from figure A1 which is taken from [25].

ORCID iDs

Jagdish A Krishnaswamy ⓘ https://orcid.org/0000-0001-7451-3237
Luis Rodriguez-Tembleque ⓘ https://orcid.org/0000-0003-2993-8361

References

[1] García-Macías E, Rodríguez-Tembleque L and Sáez A 2018 MWCNT/epoxy strip-like sensors for buckling detection in beam-like structures *Thin-Walled Struct.* **133** 27–41

[2] Maurya D, Peddigari M, Kang M-G, Geng L D, Sharpes N, Annapureddy V, Palneedi H, Sriramdas R, Yan Y and Song H-C 2018 Lead-free piezoelectric materials and composites for high power density energy harvesting *J. Mater. Res.* **33** 2235–63

[3] Ibn-Mohammed T, Koh S, Reaney I, Sinclair D, Mustapha K, Acquaye A and Wang D 2017 Are lead-free piezoelectrics more environmentally friendly? *MRS Commun.* **7** 1–7

[4] Topolov V Y, Bisegna P and Bowen C R 2014 *Orientation Effects and Anisotropy Factors* (Berlin: Springer) (https://doi.org/10.1007/978-3-642-38354-0)

[5] Yuan R, Liu Z, Balachandran P V, Xue D, Zhou Y, Ding X, Sun J, Xue D and Lookman T 2018 Accelerated discovery of large electrostrains in BaTiO₃-based piezoelectrics using active learning *Adv. Mater.* **30** 1702884

[6] Alluri N R, Selvarajan S, Chandrasekhar A, Saravanakumar B, Lee G M, Jeong J H and Kim S-J 2017 Worm structure piezoelectric energy harvester using ionotropic gelation of barium titanate-calcium alginate composite *Energy* **118** 1146–55

[7] Roscow J I, Lewis R W C, Taylor J and Bowen C R 2017 Modelling and fabrication of porous sandwich layer barium titanate with improved piezoelectric energy harvesting figures of merit *Acta Mater.* **128** 207–17

[8] Alluri N R, Chandrasekhar A, Vivekananthan V, Purusothaman Y, Selvarajan S, Jeong J H and Kim S-J 2017 Scavenging biomechanical energy using high-performance, flexible BaTiO₃ nanocube/PDMS composite films *ACS Sustain. Chem. Eng.* **5** 4730–8

[9] Shi K, Huang X, Sun B, Wu Z, He J and Jiang P 2019 Cellulose/BaTiO₃ aerogel paper based flexible piezoelectric nanogenerators and the electric coupling with triboelectricity *Nano Energy* **57** 450–8

[10] Wang D, Du H, Wang L and Melnik R 2018 A phase field approach for the fully coupled thermo-electro-mechanical dynamics of nanoscale ferroelectric actuators *Smart Mater. Struct.* **27** 055012

[11] Kim H, Torres F, Villagran D, Stewart C, Lin Y and Tseng T L B 2017 3D printing of BaTiO₃/PVDF composites with electric *in situ* poling for pressure sensor applications *Macromol. Mater. Eng.* **302** 1700229

[12] Kim H, Wilburn B R, Castro E, Garcia Rosales C A, Chavez L A, Tseng T-L B and Lin Y 2018 Multifunctional SENSING using 3D printed CNTs/BaTiO₃/PVDF nanocomposites *J. Compos. Mater.* **53** 1319–28

[13] Kim K, Zhu W, Qu X, Aaronson C, McCall W R, Chen S and Sirbuly D J 2014 3D optical printing of piezoelectric nanoparticle–polymer composite materials *ACS Nano* **8** 9799–806

[14] Dudem B, Kim D H, Bharat L K and Yu J S 2018 Highly-flexible piezoelectric nanogenerators with silver nanowires and barium titanate embedded composite films for mechanical energy harvesting *Appl. Energy* **230** 865–74

[15] Agnelli F, Constantinescu A and Nika G 2018 Optimal design of auxetic, additively manufactured, polymeric structures arXiv:1809.02467

[16] Phatharapeetranun N, Ksapabutr B, Marani D, Bowen J R and Esposito V 2017 3D-printed barium titanate/poly-(vinylidene fluoride) nano-hybrids with anisotropic dielectric properties *J. Mater. Chem.* C **5** 12430–40

[17] Kim H, Torres F, Islam M T, Islam M D, Chavez L A, Rosales C A G, Wilburn B R, Stewart C M, Noveron J C and Tseng T-L B 2017 Increased piezoelectric response in functional nanocomposites through multiwall carbon nanotube interface and fused-deposition modeling three-dimensional printing *MRS Commun.* **7** 960–6

[18] Wang X 2012 Piezoelectric nanogenerators—harvesting ambient mechanical energy at the nanometer scale *Nano Energy* **1** 13–24

[19] Majdoub M S, Sharma P and Cagin T 2008 Enhanced size-dependent piezoelectricity and elasticity in nanostructures due to the flexoelectric effect *Phys. Rev.* B **77** 125424

[20] Majdoub M S, Sharma P and Çağin T 2008 Dramatic enhancement in energy harvesting for a narrow range of dimensions in piezoelectric nanostructures *Phys. Rev.* B **78** 121407

[21] Maranganti R and Sharma P 2009 Atomistic determination of flexoelectric properties of crystalline dielectrics *Phys. Rev.* B **80** 054109

[22] Saputra A A, Sladek V, Sladek J and Song C 2018 Micromechanics determination of effective material coefficients of cement-based piezoelectric ceramic composites *J. Intell. Mater. Syst. Struct.* **29** 845–62

[23] Qin R-S, Xiao Y and Lan H 2014 Numerical simulation of effective properties of 3d piezoelectric composites *J. Eng.* **2014** 824806

[24] Sladek J, Sladek V, Krahulec S and Song C 2016 Micromechanics determination of effective properties of voided magnetoelectroelastic materials *Comput. Mater. Sci.* **116** 103–12

[25] Charalambakis N 2010 Homogenization techniques and micromechanics. A survey and perspectives *Appl. Mech. Rev.* **63** 030803

[26] Zheng P, Zhang J, Tan Y and Wang C 2012 Grain-size effects on dielectric and piezoelectric properties of poled BaTiO$_3$ ceramics *Acta Mater.* **60** 5022–30

[27] Li J Y 2000 The effective electroelastic moduli of textured piezoelectric polycrystalline aggregates *J. Mech. Phys. Solids* **48** 529–52

[28] Jayachandran K P, Guedes J M and Rodrigues H C 2009 Effect of microstructure and texture on the macroscopic piezoelectric response of ferroelectric barium titanate and PZN-PT films *J. Intell. Mater. Syst. Struct.* **20** 193–204

[29] Johnston I, McCluskey D, Tan C and Tracey M 2014 Mechanical characterization of bulk Sylgard 184 for microfluidics and microengineering *J. Micromech. Microeng.* **24** 035017

[30] Tjernlund J A, Kristofer Gamstedt E and Gudmundson P 2006 Length-scale effects on damage development in tensile loading of glass-sphere filled epoxy *Int. J. Solids Struct.* **43** 7337–57

[31] Soh A and Liu J X 2005 On the constitutive equations of magnetoelectroelastic solids *J. Intell. Mater. Syst. Struct.* **16** 597–602

[32] Melnik R V N 2000 Generalised solutions, discrete models and energy estimates for a 2D problem of coupled field theory *Appl. Math. Comput.* **107** 27–55

[33] Babu I and de With G 2014 Highly flexible piezoelectric 0–3 PZT–PDMS composites with high filler content *Compos. Sci. Technol.* **91** 91–7

[34] Ren K, Liu Y, Geng X, Hofmann H F and Zhang Q M 2006 Single crystal PMN-PT/epoxy 1–3 composite for energy-harvesting application *IEEE Trans. Ultrason. Ferroelectr. Freq. Control* **53** 631–8

[35] Raponi O D A, Raponi R D A, Barban G B, Benedetto R M D and Ancelotti Junior A C 2017 Development of a simple dielectric analysis module for online cure monitoring of a commercial epoxy resin formulation *Mater. Res.* **20** 291–7

[36] Bowen C R, Dent A C, Stevens R, Cain M G and Avent A 2017 A new method to determine the un-poled elastic properties of ferroelectric materials *Sci. Technol. Adv. Mater.* **18** 264–72

[37] Berlincourt D and Jaffe H 1958 Elastic and piezoelectric coefficients of single-crystal barium titanate *Phys. Rev.* **111** 143

[38] Zgonik M, Bernasconi P, Duelli M, Schlesser R, Günter P, Garrett M H, Rytz D, Zhu Y and Wu X 1994 Dielectric, elastic, piezoelectric, electro-optic, and elasto-optic tensors of BaTiO$_3$ crystals *Phys. Rev.* B **50** 5941–9

[39] Kratzer M, Lasnik M, Röhrig S, Teichert C and Deluca M 2018 Reconstruction of the domain orientation distribution function of polycrystalline PZT ceramics using vector piezoresponse force microscopy *Sci. Rep.* **8** 422

[40] Maurya D, Zhou Y, Yan Y and Priya S 2013 Synthesis mechanism of grain-oriented lead-free piezoelectric Na0.5Bi0.5TiO$_3$-BaTiO$_3$ ceramics with giant piezoelectric response *J. Mater. Chem.* C **1** 2102–11

[41] Gaiser P, Binz J, Gompf B, Berrier A and Dressel M 2015 Tuning the dielectric properties of metallic-nanoparticle/elastomer composites by strain *Nanoscale* **7** 4566–71

[42] Pecharroman C, Esteban-Betegon F, Bartolome J F, Lopez-Esteban S and Moya J S 2001 New percolative BaTiO$_3$–Ni composites with a high and frequency-independent dielectric constant (ϵr $\approx$ 80000) *Adv. Mater.* **13** 1541–4

[43] Roscow J I, Bowen C R and Almond D P 2017 Breakdown in the case for materials with giant permittivity? *ACS Energy Lett.* **2** 2264–9